Thin film structural analysis using variable-period x-ray standing waves

Joshua S. Gibson,[1] Karen L. Syres,[1,*] Matthew Buckley,[1] Tien-Lin Lee,[2] Pardeep K. Thakur,[2] and Robert G. Jones[1,†]
[1]*School of Chemistry, University of Nottingham, Nottingham NG7 2RD, United Kingdom*
[2]*Diamond House, Harwell Science and Innovation Campus, Didcot, Oxfordshire OX11 0DE, United Kingdom*

(Received 26 September 2017; revised manuscript received 12 December 2017; published 1 October 2018)

Variable-period x-ray standing wave (VPXSW) studies have been carried out using 3 keV x rays and photoelectron detection. Two model surfaces have been used, a native SiO_2 layer (20 Å thick) on bulk silicon, and a purpose-built multilayer surface comprising a chloroform/water marker layer (12 Å thick) on an ionic liquid spacer layer (211 Å thick) deposited on a SiO_2/Si substrate at 90 K. By using photoelectron detection, both chemical and elemental sensitivity were achieved. The surfaces were modeled using dynamic x-ray scattering for x-ray intensity, and attenuation of photoelectrons transmitted through the layers, to produce simulations which accurately reproduced the experimental VPXSW measurements. VPXSW measurements made using the substrate, spacer layer, and marker layer photoelectron signatures produced consistent structural values. This work demonstrates that VPXSW can be used to determine chemically specific layer thicknesses within thick ($\lesssim$300 Å) surface structures composed of the light elements B, C, N, O, F, and Cl with an accuracy of 10 to 15 Å, perpendicular to the surface.

DOI: 10.1103/PhysRevB.98.165402

I. INTRODUCTION

The techniques available for determining the composition of thin films 1–50 nm thick, as a function of depth, are currently rather limited. Ellipsometry [1–3] provides thickness and dielectric information, while x-ray reflectivity [4] provides thickness and the electron density profile perpendicular to the surface. Chemical species identification can be achieved by ion-stripping methods coupled with analysis—for example, secondary-ion mass spectrometry (SIMS) [5] or photoelectron spectroscopy with ion etching—but these are inherently destructive and the depth resolution is degraded by roughening. Angle-resolved x-ray photoelectron spectroscopy (ARXPS) can map depth distributions of chemically identifiable species, but the resolution of $\approx 0.81z$ [6], where z is the depth, is rather low. X-ray standing wave (XSW) fields have been used to determine surface atomic positions [7], and fall into two categories. (i) Photoelectrons, Auger electrons, and secondary electrons have been used as the detection method for XSWs formed by Bragg reflection from crystalline samples to measure positions with high precision (0.02 Å) over rather short ranges (<1 nm) [7,8], or over somewhat longer ranges using synthetic multilayer crystals [9,10]. (ii) X-ray fluorescence detected variable-period XSW, where the standing wave is formed by reflection from a flat surface, has been used to measure positions over much longer scales, 10–100s nm [7,11], but only with elemental sensitivity.

X-ray standing waves have been used over the past several decades for structural analysis of both bulk solids and surfaces [7]. Generally a standing wave is formed when two waves of the same wavelength and a given phase relationship cross. An x-ray standing wave can be formed by x-ray diffraction [7,12–16], where the incident and diffracted x-ray beams overlap. For Bragg diffraction, $\lambda = 2d_{hkl}\sin\theta$, where λ is the x-ray wavelength, d_{hkl} the spacing of the (hkl) set of planes, and θ the angle of incidence and reflection. The standing wave intensity has a fixed periodicity of d_{hkl} along the normal to the (hkl) planes. The phase difference between the incident and diffracted beam at the Bragg condition is changed by either scanning θ over a small angular range for a fixed λ (normally referred to as XSW), or by scanning λ (i.e., the x-ray energy) slightly for a fixed θ. For the latter, θ is often set to 90° and is known as normal-incidence x-ray standing wave (NIXSW) where the sine function is at a turning point making the technique relatively insensitive to crystal imperfections, and hence applicable to rather poor crystals such as metal crystals. To the low-energy side of the Bragg condition, only the incident x-ray beam exists as a travelling wave passing through the sample. As the Bragg condition is approached, the diffracted beam comes into existence and forms the standing wave with the nodes located on the (hkl) planes and the antinodes halfway between. As the Bragg condition is traversed, the phase relationship changes shifting the position of the standing wave until the antinodes are on the (hkl) planes and the nodes are halfway between. On the high-energy side of the Bragg condition, the diffracted beam disappears, leaving just the incident beam passing through the sample. The standing wave exists both inside and outside the crystal and its intensity and position can be accurately calculated using dynamical x-ray theory. The standing wave is the "ruler" by which atomic positions are measured by monitoring the photoelectrons, Auger electrons, secondary electrons, and fluorescence x-ray photons from atoms within the wave field. By monitoring the intensity of these emissions, the positions of the atoms within

*Current address: Jeremiah Horrocks Institute, University of Central Lancashire, Fylde Road, Preston PR1 2HE, UK.

†Author to whom correspondence should be addressed: robert.g.jones@nottingham.ac.uk

 ©2018 American Physical Society

the x-ray wave field are determined, and hence the positions relative to the (hkl) planes. However, as the standing wave is periodic in d_{hkl}, atomic positions at md_{hkl}, where m is an integer, are indistinguishable, so other information such as known atomic sizes and bond lengths have to be used to determine distances greater than d_{hkl}. One way to increase d_{hkl} is to use synthetic layered materials and this has been successfully applied [9,10].

An alternative way to form an x-ray standing wave is to reflect x rays from a polished surface such that the incident and reflected waves overlap above the surface [11,17–25]. To achieve a reflected x ray of sufficient intensity to form the standing wave, the angle of incidence, α, has to be in the region of the critical angle, α_{crit}, of the surface. By scanning the incident angle from 0 to a few times α_{crit}, an x-ray standing wave is produced above the surface which starts with an intensity period of ∞, but then falls to a period of $\approx$100 Å at α_{crit} and continues decreasing for larger angles. The period is therefore variable, depending on the angle of incidence. Such variable-period x-ray standing wave (VPXSW) studies, also known as grazing-incidence x-ray standing waves (GIXSWs), were first realized in 1989 [17] and can probe thicknesses of 10–100 nm with a spatial resolution of $\approx$0.2 nm, which is $\approx$10 to 100 times the thickness accessible to diffraction-based XSW.

Experiments have been carried out since the mid-1970s to explore the possibilities of combining photoelectron spectroscopy and grazing-incidence reflection. Early work by Mehta and Fadley [26,27] established that the enhanced electric field at grazing incidence increased the relative sensitivity of surface species in XPS. Kawai *et al.* [28] carried out total reflection x-ray photoelectron spectroscopy (TRXPS) and presented a kinematical theory for the evanescent x-ray wave in the substrate surface region leading to enhanced surface sensitivity in XPS. This enhanced XPS surface sensitivity was further explored using Si samples [29] and copper phthalocyanine on Si [30] and in a review of TRXPS [31] Kawai points out the possibilities of using x-ray standing waves monitored by photoelectron emission for thin film measurements. Chester *et al.* used grazing-incidence XPS (GIXPS) to enhance surface sensitivity of XPS and presented a dynamical x-ray theory to calculate x-ray intensities within the substrate and adlayers [32,33]. This was used to study relatively thin ($\lesssim$50 Å thick) gold films on Si surfaces, and oxide layers ($\lesssim$70 Å thick) on GaAs, and it was noted that GIXPS would be a valuable tool for nondestructive depth profiling that is amenable to quantitation. Jach *et al.* have gone on to apply GIXPS to thin oxide layers ($\lesssim$75 Å) on Si [34,35,36] and also oxynitride layers [37] ($\lesssim$50 Å) on Si.

In this work we demonstrate that it is possible to quantitatively determine the structure of a thick film ($\lesssim$250 Å) using several periods of an x-ray standing wave setup by reflection from a buried interface, in the manner of GIXSW, using photoelectron detection rather than x-ray fluorescence to achieve chemical state specificity via the photoelectron chemical shift [38]. This eliminates the need for a crystalline substrate, greatly lengthens the analysis range, and provides more structural information than the single period from Bragg diffraction. We demonstrate, using this technique, that the thickness of a thick molecular film composed of the light elements B, C, N, and F may be determined (211 $\pm$ 15 Å). We also show that it is possible to determine the position of a thin marker layer (12 $\pm$ 10 Å thick) containing other light elements O and Cl residing on the outside of the thick organic film. This work is a demonstration that VPXSW can be used as a viable structural tool for the analysis of thick films up to 250 Å with chemical state specificity.

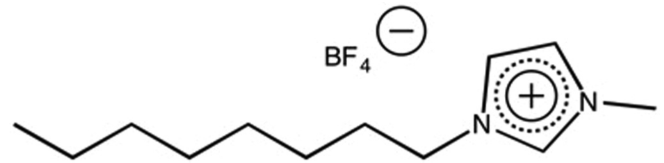

FIG. 1. Structure of [OMIM][BF_4].

To test and compare the spatial resolution and ability to detect light elements two model films were used. The first consisted of a silicon wafer covered by its inherent thin layer oxide surface. The second comprised a thick test film built in vacuum at 90 K on the oxide-covered silicon wafer. It consisted of an organic "spacer" layer of ionic liquid (IL), 1-octyl-3-methylimidazolium tetrafluoroborate, [OMIM][BF_4], Fig. 1, grown to a depth of $\approx$200 Å with a thin marker layer of chloroform ($CHCl_3$) and water, adsorbed on top of it. VPXSW experiments were carried out while monitoring the photoemission signals from Si, O, C, N, F, B, and Cl. The results for the first sample, Si/SiO_2, found that the oxide layer was 20 $\pm$ 10 Å thick, with VPXSW data from silicon photoemission from the bulk and silicon and oxygen photoemission from the oxide being fully consistent. Analysis of the marker layer showed the $CHCl_3 - H_2O$ layer to be 12 $\pm$ 10 Å thick, with its outer surface located 223 $\pm$ 15 Å from the surface, while analysis of the IL spacer layer signals showed a layer of IL 211 $\pm$ 15 Å thick with a marker layer 12 $\pm$ 10 Å thick (containing $CHCl_3$ and H_2O) on top of it. Also VPXSW data obtained from silicon photoemission from the bulk and SiO_2 layers below the organic layer were fitted with the same structural parameters as used for the marker and spacer layers; see Fig. 6(b). This demonstrates that adlayers on the order of 100s Å can be structurally analyzed with an accuracy of 10–15 Å.

II. THEORY AND SIMULATIONS

We have followed Zhang [25] in calculating the x-ray amplitude and hence intensity for positions within the standing wave and hence within the adlayer. We use a three-layer model where the vacuum is layer 1, the adlayer is layer 2, and the substrate is layer 3, Fig. 2. The refractive index, n, of a medium for x rays is given by

$$n = 1 - \delta - i\beta, \tag{1}$$

where β is the absorption index and δ is the refractive index decrement. As n is less than 1, total external reflection occurs for incident angles, α, smaller than the critical angle, α_c, given to a good approximation by

$$\alpha_c \approx (2\delta)^{1/2}. \tag{2}$$

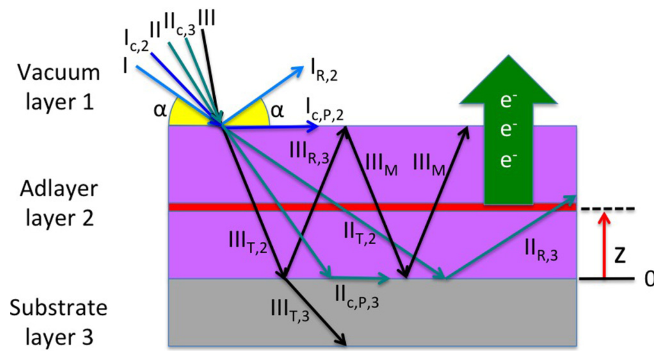

FIG. 2. X-ray standing wave formation. Schematic of the behavior of x rays incident on a three-layer surface comprising a vacuum (layer 1), adlayer (layer 2), and substrate (layer 3) as the incident angle, α, is increased from 0. Various rays are shown (I, $I_{c,2}$, II, $II_{c,3}$, III), where P = parallel, R = reflected, T = transmitted, M = multiple reflections, c = critical angle, and 1, 2, 3 refer to the higher layer number at an interface where P, R, or T occurs. A thin layer at position z in layer 2 is shown emitting photoelectrons (large green arrow).

For layer 1 (vacuum) the x-ray constants β and δ are zero, and for layers 2 and 3 they were calculated [39] for the material and the x-ray energy used (3000 eV). For the first sample, the adlayer, layer 2, was SiO_2 with $\beta_2 = 4.1625 \times 10^{-6}$ and $\delta_2 = 5.174 \times 10^{-5}$, giving a critical angle of $\alpha_{2,\text{crit}} = 0.5828^\circ$ and the substrate, layer 3, was Si with $\beta_3 = 7.4498 \times 10^{-6}$ and $\delta_3 = 5.4303 \times 10^{-5}$, giving a critical angle of $\alpha_{3,\text{crit}} = 0.5971^\circ$. For the second sample the adlayer was primarily the ionic liquid with a marker layer consisting of $CHCl_3$ and H_2O. We will refer to the $CHCl_3$-H_2O-IL adlayer as the organic layer, sitting on the substrate, layer 3, which consisted of a thin layer of SiO_2 on bulk Si. For the purposes of calculating the x-ray intensity within the adlayer, the values of δ for the IL, $CHCl_3$, and water for 3 keV x rays are sufficiently close (see Sec. A in the Supplemental Material [40]) that they can be considered to be the same. We have therefore used the values of the IL, $\beta_2 = 5.1271 \times 10^{-6}$, $\delta_2 = 2.7828 \times 10^{-5}$, giving $\alpha_{2,\text{crit}} = 0.4274^\circ$. Similarly, for layer 3, the SiO_2 layer is thin and its δ value is sufficiently similar to Si, and both are sufficiently different from the organic values, that the Si values were used for layer 3; see Sec. A in the Supplemental Material [40] for more information. Using these constants and the angle of incidence, α, the x-ray intensity can be calculated at any position, z, measured from the substrate/adlayer interface into the adlayer, as well as the intensity within the substrate layer and in the vacuum.

Figure 3(a) shows the x-ray intensity, normalized to the intensity of the incident wave, versus angle for positions z along the surface normal for the simplest case where layers 1 and 2 are both vacuum above layer 3 which is a clean silicon surface. For increasing α the x-ray intensity at $z = 0$ rises to a maximum at the critical angle of the silicon, $\alpha_{3,\text{crit}} = 0.597^\circ$, and then decays to an intensity corresponding to a traveling x-ray wave propagating into the silicon bulk (=1). Below the critical angle total external reflection occurs with a reflected wave above the surface and an evanescent wave propagating into the silicon. At the critical angle the reflected wave is at maximum intensity and a refracted wave forms, traveling along the silicon surface which causes the maximum in the standing wave intensity at $z = 0$. Above the critical angle a refracted wave propagates into the bulk while a reflected wave propagates into the vacuum. The incident and reflected waves combine above the surface to form a standing wave of intensity versus z for any given α. For a position $z = 250$ Å out from the surface, five x-ray nodes and antinodes sweep past the position as α scans from 0° to 2°, while for smaller value of z appropriately reduced modulations of x-ray intensity are experienced. Species at different distances z will experience different standing waves, which is the "ruler" for this structural technique. For large angles the reflected wave intensity drops to zero causing the standing wave to disappear.

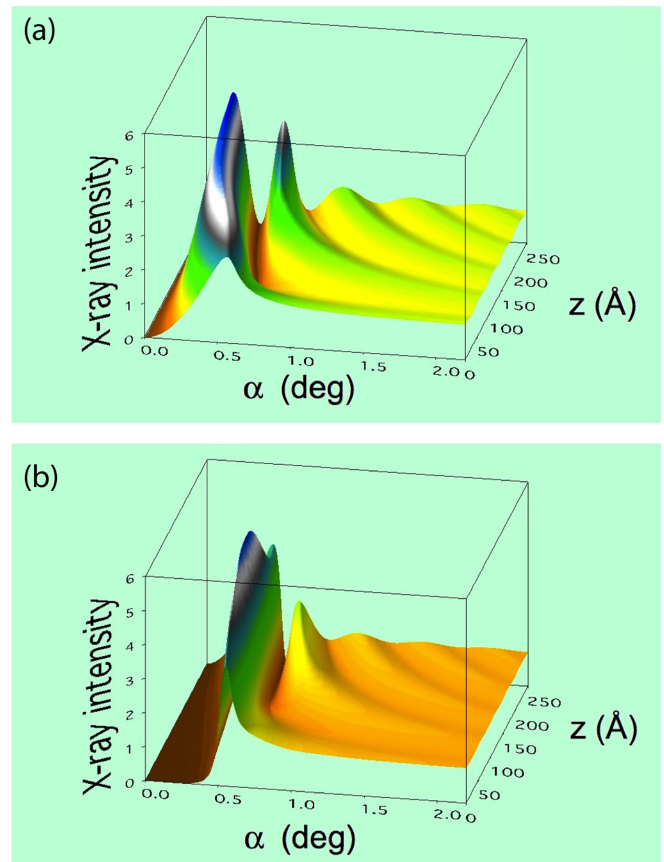

FIG. 3. Calculated x-ray intensity versus angle α and position z within layer 2 at an x-ray energy of 3000 eV. (a) For a clean Si surface where layer 2 is vacuum. (b) For a 250 Å thick slab of $[OMIM][BF_4]$, layer 2, on a silicon substrate, layer 3.

Figure 3(b) shows the effect on the x-ray intensity for a 250 Å thick organic layer of the IL (layer 2) on Si (layer 3), Fig. 2. For the ionic liquid the critical angle of the adlayer $\alpha_{c,\text{org}} = 0.427^\circ$. Hence for incident angles $0 \leqslant \alpha < \alpha_{c,\text{org}}$ x rays reflect from the top of layer 2 ($z = 250$ Å), ray I-$I_{R,2}$, Fig. 2. The x-ray intensity at the layer 1/layer 2 interface increases with increasing α while the intensity of the evanescent wave that penetrates below the interface, Fig. 3(b), decreases as z decreases towards the bottom of layer 2, such that there is almost no intensity at the layer 2/layer 3 interface at $z = 0$. For $\alpha = \alpha_{c,\text{org}}$ (ray $I_{c,2}$) there is a reflected wave, and a transmitted

wave (ray $I_{c,P,2}$) which is located at, and runs parallel to, the layer 1/layer 2 interface, giving a maximum intensity at $z = 250$ Å. For incident angles that lie between the critical angles of the adlayer and the substrate, $\alpha_{c,\mathrm{org}} < \alpha < \alpha_{c,\mathrm{Si}}$, Fig. 2, II, the transmitted wave now propagates through layer 2 towards the layer 2/layer 3 interface (ray $II_{T,2}$) where it reflects (ray $II_{R,3}$) from layer 3 (silicon), for which the critical angle is $\alpha_{c,\mathrm{Si}} = 0.597^\circ$. The waves $II_{T,2}$ and $II_{R,3}$ form a standing wave within the adlayer, with an evanescent wave penetrating a short distance into the silicon. When $\alpha = \alpha_{c,\mathrm{Si}}$, ray $II_{c,3}$, another transmitted wave is formed at, and running parallel to, the layer 2/layer 3 interface, ray $II_{c,P,3}$, giving a maximum intensity at $z = 0$, Fig. 3(b). For $\alpha > \alpha_{c,\mathrm{Si}}$ x rays are partially reflected (ray $III_{R,3}$) and partially transmitted (ray $III_{T,3}$) by the substrate, the two waves $III_{T,2}$ and $III_{R,3}$ continuing to form a standing wave within layer 2. Eventually, as α increases the reflected wave decreases in intensity until there is simply a traveling wave passing through the entire surface. As can be seen from Fig. 3(b), at any particular value of $\alpha > \alpha_{c,\mathrm{Si}}$ there is an x-ray standing wave intensity with a period and an intensity that decreases as α increases. Multiple reflections within the adlayer (rays III_M in Fig. 2) modify the intensity of the standing wave substantially, causing higher and lower intensities than those found above the clean surface. The x-ray intensity within layer 3, the silicon substrate, can also be calculated and depends on the nature of layer 2 above it. Hence for quantitative results, the surface should be considered as a whole when calculating the standing wave.

X-ray absorption at position z is proportional to the x-ray intensity, and to the number density of absorbing species, at that position. Hence the photoelectron intensity generated at position z, and the hole density, will be proportional to x-ray intensity and the number density of the emitting species. Also the x-ray fluorescence intensity and Auger electron intensity generated from hole decay traveling towards a detector are proportional to the x-ray intensity and number density of emitting species at z. The intensity of these emissions emerging from the surface of layer 2 is given by the Beer-Lambert law which for photoelectrons traveling along the surface normal can be written

$$I_e/I_{e0} = \exp[-(d_2 - z)/\lambda], \tag{3}$$

where I_{e0} is the photoelectron intensity at position z (valid for $0 < z < d_2$) traveling towards the analyzer, I_e is the photoelectron flux emerging into vacuum, d_2 is the thickness of layer 2, and λ is the attenuation length for the particular electron kinetic energy of the emission traveling through layer 2. The measurable quantity is I_{exp}, the integral of I_e over the distribution of species (from position z_1 to z_2) within the adlayer,

$$I_{\mathrm{exp}} = \int_{z_1}^{z_2} I_e dz. \tag{4}$$

To simulate the VPXSW curves, the substrate, layer 3, was considered to be of uniform density having x-ray constants β_3 and δ_3. The adlayer, layer 2, was of uniform density, of thickness d_2, with x-ray constants β_2 and δ_2. Photoelectron emission towards the surface, along the surface normal, was allowed to occur from a photoelectron region within layer 2, having a relative density $\rho(z)$ of photoelectron-emitting species, with its center at position z_0 from the substrate surface, and of thickness t, i.e., from $z_0 - t/2$ to $z_0 + t/2$. The photoelectron region can be either a marker layer, a spacer layer, or the whole of layer 2, depending on the values of z_0 and t. At each incident angle α, the intensity of the x-ray standing wave, $I(z)$, was calculated at each position z through the photoelectron region. The photoelectron intensity for a given species at position z was then calculated using

$$I_{e0}(z) \propto \rho(z) I(z) \delta z, \tag{5}$$

where δz is the thickness element; in this work $\delta z = 1$ Å. The photoelectron flux, $I_e(z)$, from δz emerging at the surface is given by Eq. (6) written explicitly with I_e and I_{e0} as functions of z,

$$I_e(z) = I_{e0}(z) \exp[-(d_2 - z)/\lambda], \tag{6}$$

where λ is the attenuation length for the photoelectron kinetic energy and the material comprising layer 2. The attenuation length, λ, was taken to be $0.8\lambda_{\mathrm{imfp}}$, where λ_{imfp} is the calculated inelastic mean free path for a particular photoelectron kinetic energy through the IL [41,42]. The measured photoelectron flux leaving the surface along the surface normal for a particular angle of incidence, Eq. (4), is then the sum of all contributions from z across the thickness t within the adlayer using increments δz,

$$I_{\mathrm{exp}} = \sum_{z_0 - t/2}^{z_0 + t/2} I_e(z) \delta z. \tag{7}$$

The calculation is repeated over the range of α used in the experiment.

To compare the simulated and experimental VPXSW data two corrections are necessary. First, the simulation is corrected for the increased path length of the x rays through the adlayer for small values of α. This is achieved by division by $\sin\alpha$ (or by just α, as the angles are small). Second, the calculated photoelectron intensity is corrected for the overlap of the x-ray footprint on the sample surface with the analysis area seen by the electron energy analyzer. When the x-ray footprint is completely within the analyzer field of view, all photoelectron intensity is captured and no correction is required. But for very low angles, the footprint falls outside the analyzer field of view and the signal is lost. The ratio of the x-ray beam diameter (d_{beam}) to the concentric hemisphere analyzer (CHA) field of view diameter (d_{anal}) is used to determine the angle, α_{FP}, at which the x-ray footprint starts to exceed the analyzer field of view ($\sin\alpha_{\mathrm{FP}} = d_{\mathrm{beam}}/d_{\mathrm{anal}}$). In this work a ratio of 0.012 was used. The correction involves multiplying the simulation intensity by $\sin\alpha_{\mathrm{FP}}/(d_{\mathrm{beam}}/d_{\mathrm{anal}})$, i.e., 1, for $\alpha \geqslant \alpha_{\mathrm{FP}}$ and by $\sin\alpha/(d_{\mathrm{beam}}/d_{\mathrm{anal}})$ for $\alpha < \alpha_{\mathrm{FP}}$. The footprint correction has the effect (after normalizing to the maximum value in the simulated VPXSW scan to 1) of reducing the photoelectron intensity at higher angles, and is used to match the simulation and experimental intensities. The abrupt change at α_{FP} can lead to a noticeable kink in the simulation (see Fig. 14), which could be smoothed if necessary. For 3000 eV x rays and $\alpha > 0.1^\circ$ there is no appreciable attenuation of the x rays as they pass through the adlayers used here; hence no correction for x-ray attenuation within the adlayer has been applied. The program used to

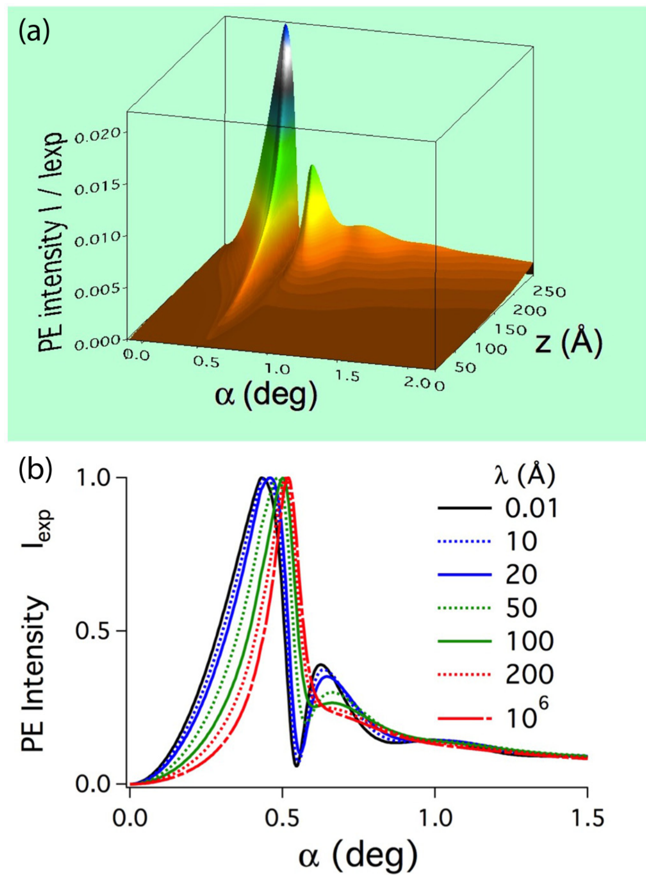

FIG. 4. (a) Fraction of photoelectron intensity, I_e/I_{exp}, emerging from the surface of layer 2, which originates from a 1 Å thick layer at position z, versus angle α calculated using $\lambda = 50$ Å. (b) Photoelectron intensity, I_{exp}, (normalised to 1 at the maximum), versus α plots for different values of the electron attenuation length λ. The $\lambda = 10^6$ Å curve is equivalent to x-ray fluorescent detection and is the same as a plot of the total hole density. Layer 2 is [OMIM][BF_4] with $d_2 = 250$ Å, layer 3 is Si, and the x-ray energy was 3000 eV. All plots are normalized to 1 at their maximum and have been corrected for the x-ray footprint and path length.

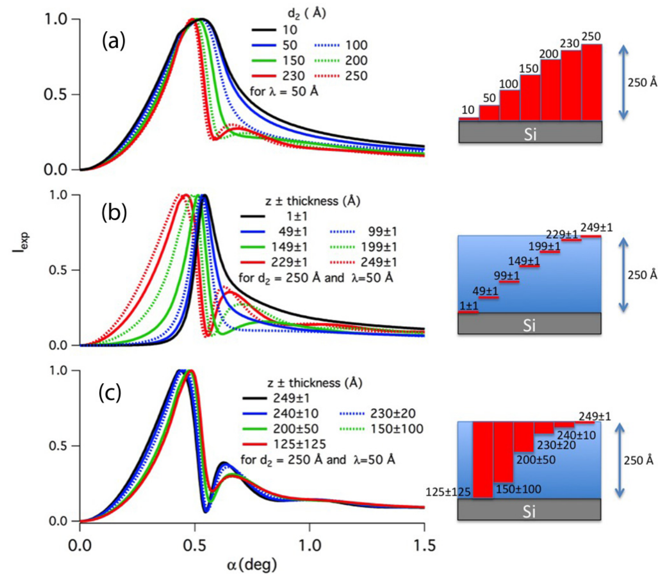

FIG. 5. Normalized photoelectron intensity I_{exp} versus α for slabs of ionic liquid of thickness d_2 containing marker layers at position z_0 with a thickness either side of z_0 of $\pm t/2$, on top of silicon, using 3000 eV x rays and $\lambda = 50$ Å. (a) I_{exp} for a slab of thickness d_2. (b) I_{exp} from a marker layer $t = 2$ Å thick ($z_0 \pm 1$ Å) at position z_0 within an IL slab of thickness 250 Å. (c) I_{exp} from marker layers of thickness 2 to 250 Å terminating at the IL/vacuum interface. Corrections for x-ray footprint and path length have been made.

calculate the VPXSW profiles is available from the authors [43].

Figure 4(a) shows I_e/I_{exp}, the photoelectron intensity originating from a depth z as a fraction of the experimentally determined signal versus α and z for an IL slab with $d_2 = 250$ Å using $\lambda = 50$ Å. This illustrates how different depths within the adlayer contribute to the experimental signal, depths less than 50 Å contributing the most, while for depths > 250 Å the signal drops to $<1\%$. Figure 4(b) shows total photoelectron intensity, I_{exp}, expected from a homogeneous slab of IL 250 Å thick (layer 2) on Si for different values of the electron attenuation length λ, each normalized to 1 for its maximum value. For large values of λ ($= 10^6$ Å) the intensity is not attenuated by its passage through layer 2 and the plot is the same as for x-ray fluorescence detection, the signal being proportional to the sum of the hole densities within the slab caused by x-ray absorption. As λ is reduced the photoelectron signal becomes increasingly dominated by a reduced thickness of material at the IL/vacuum interface. This causes the leading edge to move to lower angle and for oscillations to grow above 0.5°, due to the material becoming sensitive to the structure of the x-ray standing wave within the surface region of the slab. For $\lambda \leqslant 10$ Å the curve tends to a limit where only the topmost part of the slab contributes to the photoelectron signal. Clearly electron detection gives a more modulated signal than x-ray fluorescence (hole density) due to the averaging effect of a large λ on the latter.

Figure 5(a) shows the total photoelectron signal, I_{exp}, versus α for slabs of [OMIM][BF_4] of total thickness, d_2, on top of silicon. The thinnest slab of 10 Å has a peak at 0.53°, slightly below the critical angle of Si ($\alpha_{\mathrm{Si,crit}} = 0.5971°$). As the thickness increases the peak moves to lower angle, the drop on the high-angle side becomes steeper, and at $d_2 = 200$ Å a second peak develops at 0.74°. As the thickness increases further the second peak becomes more intense and moves to lower angles while the first peak continues shifting towards the critical angle of the IL ($\alpha_{\mathrm{org,crit}} = 0.4274°$). Only minor changes occur in the leading edge. This behavior may be interpreted as the x rays penetrating the thin slab and reflecting from the IL/Si interface at the critical angle of the Si, causing the peak. As the slab gets thicker more reflection occurs from the vacuum/IL adlayer interface causing the peak to move towards the critical angle of the IL. For greater thickness two standing wave maxima sweep through the vacuum/IL interface causing the second peak at higher angle. Of relevance to the analysis below is that the plots for 230 Å and 250 Å are clearly distinguishable, the limit of distinguishability in the region of the second peak being about ± 10 Å.

Figure 5(b) shows I_{exp} which originates from thin marker layers of $t = 2$ Å thickness centered at position z_0 within an IL adlayer of total thickness $d_2 = 250$ Å. For the marker layer at $z_0 = 1$ Å there is a single peak at just below the critical angle of the Si. As the marker layer moves away from the IL/Si interface, for increasing z_0, the peak moves to lower angles, as it encounters the maximum in the x-ray standing wave further away from the Si surface at smaller angles. Simultaneously the leading edge extends to lower angles as the marker layer encounters more of the evanescent wave propagating down from the IL/vacuum surface. At $z_0 = 199$ Å a second peak appears at 0.805°, due to the marker layer being sufficiently far out that a second maximum in x-ray intensity can sweep through its position. As the z_0 position increases further toward the top of the IL layer this second peak moves to smaller angles, and for $z_0 = 230$ Å a third peak appears at 1.05° where the third antinode of the standing wave passes through the marker layer. The curves for the marker layers are more modulated than those of the thick slabs. Comparing the 229 and 249 Å curves, the position of thin marker layers should be locatable to ±5 Å.

To determine the sensitivity to layer thickness, Fig. 5(c) shows I_{exp} versus α for increasing thicknesses of marker layers at positions $z_0 \pm t/2$ within the $d_2 = 250$ Å slab of the IL. The marker layers all terminate at the IL/vacuum interface and become thicker towards the silicon surface. As the data are dominated by the material closest to the vacuum all the curves are similar. For thin layers (248 ± 1 Å and 240 ± 10 Å) the error in thickness is about ±10 Å, while for thick layers (200 ± 50 and 125 ± 125) it is about ±35 Å.

III. EXPERIMENTAL DETAILS

Experiments were carried out on beamline I09 at the Diamond Light Source, UK. The first sample was a silicon substrate (10 × 10 × 1 mm) with a thin native oxide on the surface, Fig. 6(a). It was cleaned by washing with acetone prior to insertion into the vacuum chamber and measurements. The second sample, Fig. 6(b), was built on the first by depositing the ionic liquid [OMIM][BF_4], Fig. 1, from an evaporator operated at 533 K [44,45], onto the silicon substrate at 90 K, followed by deposition of the two marker layer materials, chloroform ($CHCl_3$) and water, by adsorption from the gas phase. The IL evaporator had been previously calibrated in units of monolayers of IL s^{-1}, where 1 monolayer corresponds to a layer ≈10 Å thick, using temperature-programmed desorption from a gold surface [45]. Deposition of ≈200 Å of the IL was followed by 5×10^{-6} mbar s exposure of $CHCl_3$ (≈10 Å thick), followed by an exposure of $\approx 1 \times 10^{-6}$ mbar s of H_2O (≈10 Å thick) adventitiously adsorbed over 2 hours from the background gases ($\approx 10^{-10}$ mbar).

The x-ray beam was at 90° to the electron energy analysis direction, and polarized with the electric field parallel to that direction; see Fig. 6(c). This geometry minimizes nondipole photoemission effects [46,47] on the photoelectron intensity. Variable-period x-ray standing wave experiments were carried out as follows. A 3000 eV x-ray beam with dimensions ≈30 μm (perpendicular to surface) × ≈ 0.3 mm (parallel to surface) impinged at an angle α to the surface. This energy was chosen as it produces high-kinetic-energy photoelectrons

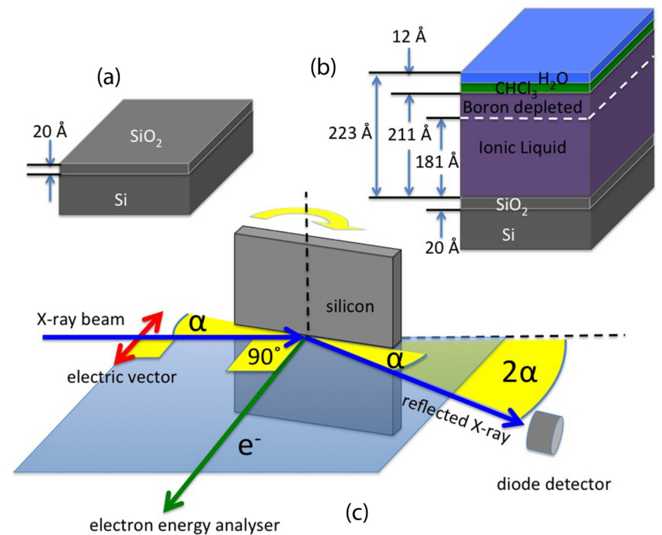

FIG. 6. (a) First sample: Silicon with native silicon oxide on the surface. (b) Second sample: Ionic liquid slab with thin marker layers of $CHCl_3$ and adventitious H_2O. (c) Schematic showing the x-ray reflection and photoelectron analysis geometry. Layer thicknesses, as determined by VPXSW, are shown in (a) and (b).

(≈2500 eV) which are penetrating ($\lambda \approx 55$ Å) but still have a photoemission cross section large enough to make the peaks easily detectable. To minimize x-ray beam damage the intensity of the x-ray beam was attenuated by 200× using slits in the beamline (20×) and by detuning the undulator gap (10×). The energy distribution curves (EDCs) of the electrons leaving the surface were measured with a concentric hemispherical analyzer (VG Scienta EW4000 10 keV, 200 mm radius hemisphere, lens acceptance angle ±30°, resolution <40 meV at 3000 eV). The CHA was operated with a pass energy of 100 eV and accepted electrons from a field of view of ≈2.5 mm diameter, giving a ratio of 0.012 for the x-ray beam size perpendicular to the surface divided by the diameter of the CHA field of view. This value is required to correct for the footprint of the x-ray beam falling outside the CHA field of view when comparing experimental and theoretical VPXSW curves. VPXSW scans were taken by scanning the incident angle α over the range 0–2.5° in steps of 0.025°, with EDCs measured at each step. Note that this angular range changes the photoelectron path length through the adlayer by <0.1% (emission angle of 90°−87.5°); hence no correction for angular-dependent attenuation of photoelectrons is required. For the first sample, clean silicon covered with native oxide, VPXSW scans were taken across the Si 2p and O 1s photoelectron peaks at 293 K. For the second sample, Si/SiO_2 substrate with an IL spacer layer and a $CHCl_3$/H_2O marker layer on top, VPXSW scans were taken at 90 K across the Si 2p, Cl 1s, C 1s, N 1s, O 1s, F 1s, and B 1s photoelectron peaks (15–30 min duration for each). To further minimize beam damage the sample was moved 0.5 mm parallel to the surface to expose fresh surface for each VPXSW scan. Even with these precautions, beam damage was observed within the adlayer.

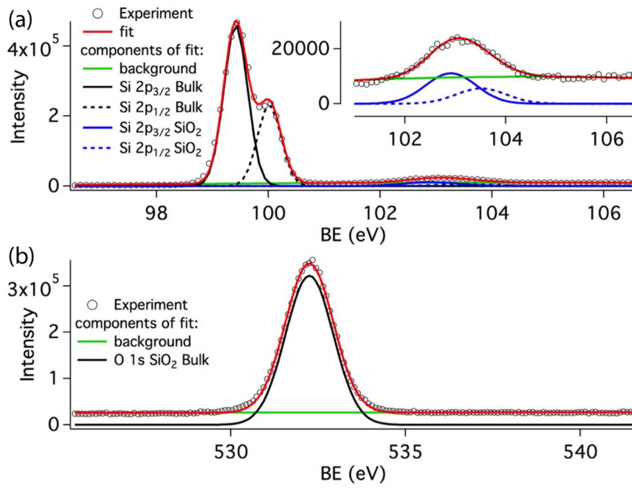

FIG. 7. Photoelectron spectra from the native oxide covered silicon surface. (a) Si $2p$ fitted using a splitting of 0.6 eV between $2p_{1/2}$ and $2p_{3/2}$, an intensity ratio of 2:1, and a chemical shift of 3.5 eV for SiO_2. Inset shows an expanded view of the SiO_2 region. (b) O $1s$ fitted with a single component. Taken at $\alpha = 2.5^\circ$.

The photoelectron peaks within each EDC were fitted using Gaussian peaks [fitting parameters: position as binding energy [BE (eV)], width [standard deviation (σ; eV)], and intensity (height or area)] on a flexible polynomial background (up to fifth order). All fitting parameters could be automatically adjusted to accommodate charging and changing chemical environments during each VPXSW scan [48]. Photoelectron peak areas, or sums of peak areas where appropriate, were then used to construct the VPXSW scans of photoelectron intensity versus angle.

IV. RESULTS AND DISCUSSION

A. First sample: Silicon substrate with native oxide

Figure 7 shows the photoelectron (PE) spectrum of the Si/SiO_2 surface at $\alpha = 2.5^\circ$. The $2p_{3/2}$ and $2p_{1/2}$ components of bulk Si and Si in SiO_2 are at binding energies (BEs) of $\approx$100 eV and $\approx$103 eV, the latter broadened due to the range of chemical environments within the surface oxide. All four components, Fig. 7(a), were fitted using Gaussian line shapes, as was the single component for the O $1s$ peak (BE = 532.3 eV), Fig. 7(b), from the SiO_2 layer. Such fitting was carried out for all the PE spectra obtained over the incident angle range of 0–2.5°. The Si $2p$ chemical shift between bulk and oxide components was 3.5 eV, slightly smaller but consistent with Refs. [49,50], which have chemical shifts of 3.7 and 4.3 eV for the unresolved $Si_{3/2,\,1/2}$ between bulk Si and the SiO_2. The fitting parameters, measured at $\alpha = 2.5^\circ$, are listed in Table I.

The VPXSW scans of photoelectron intensities versus angle of incidence, normalized to a value of 1 at their maximum, are shown in Fig. 8. The scans obtained using the Si $2p_{3/2}$ and $2p_{1/2}$ components of bulk Si are the same to within experimental error, as expected, with a peak at the critical angles of the Si and SiO_2. The shapes of the scans of the two Si components and the O $1s$ component from SiO_2 are also within error of each other, as expected if they sense the same standing wave within the oxide layer. The three curves from SiO_2 have a leading edge that rises more quickly than the bulk curves, because they encounter the standing wave earlier (at lower α). Figure 8 also shows a simulated VPXSW curve for the oxide species, corrected for the x-ray footprint and path length, for an oxide thickness of 20 Å and $\lambda = 58$ Å for Si $2p$ photoelectron transmission through the SiO_2. The fit is rather good over the entire range of 2.5°, indicating

TABLE I. Photoelectron kinetic and binding energies and calculated attenuation lengths.

Core level	Binding energy[a] (eV)	Photoelectron kinetic energy[b] (eV)	IMFP and λ[c] [51] (Å)	Width σ[d] (eV)
Cl $1s_{CHCl_3}$	2823.2(1)	≈177	11, 9	1.6(1)
Cl $1s_{Cl^-}$	2820.9(1)	≈177	11, 9	1.3(1)
Cl $1s_{Cl\bullet}$	2825.6(1)	≈177	11, 9	1.6(1)
F $1s_{anion}$	686.3(1)	≈2314	61, 49	1.4(1)
O $1s_{H_2O}$	533.4(1)	≈2468	64, 51	1.4(1)
O $1s_{damage}$	531.2(1)	≈2468	64, 51	1.0(1)
O $1s_{SiO_2}$	532.3(1)	≈2468	64, 51	1.0(1)
N $1s_{cation}$	401.6(1)	≈2598	66, 53	1.4(1)
N $1s_{damage}$	399.6(1)	≈2598	66, 53	1.5(1)
C $1s_{alkyl}$	284.9(1)	≈2715	68, 54	1.1(1)
C $1s_{hetero}$	286.5(1)	≈2715	68, 54	1.5(1)
B $1s$	194.2(1)	≈2806	70, 56	1.1(1)
Si $2p_{1/2\,bulk}$	100.0(1)	≈2901	72, 58	0.3(1)
Si $2p_{3/2\,bulk}$	99.4(1)	≈2901	72, 58	0.3(1)
Si $2p_{1/2\,SiO_2}$	103.5(1)	≈2901	72, 58	0.7(1)
Si $2p_{3/2\,SiO_2}$	102.9(1)	≈2901	72, 58	0.7(1)

[a]Single-point calibration using Si $2p_{3/2} = 99.42$ eV BE [52]. Measured at $\alpha = 2.5^\circ$.
[b]Calculated using an x-ray energy of 3000 eV.
[c]IMFP is the inelastic mean free path; λ is the attenuation length = 0.8 × IMFP. An average value of λ = 55 Å was used for all photoelectrons except Cl $1s$.
[d]σ is the standard deviation of the Gaussian peak used for fitting.

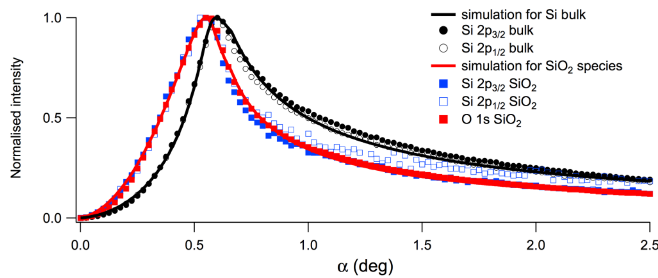

FIG. 8. VPXSW scans of the O 1s, Si 2$p_{1/2}$, and Si 2$p_{3/2}$ for Si bulk and SiO_2. The simulations (normalized to 1, corrected for footprint and path length, and shifted by 0.025°) are for an oxide layer 20 Å thick; see cartoon in Fig. 6(a).

that the theory generally, and the correction for path length in particular, is correct. Also shown in Fig. 8 is a simulated VPXSW curve for the bulk Si substrate, calculated using the same oxide thickness of 20 Å, and $\lambda = 58$ Å for photoelectron transmission through the bulk Si and SiO_2 (using $\lambda = 51$ Å for transmission of O 1s photoelectrons through SiO_2 has no significant effect on the data). The fit to the experimental data is again rather good. Both simulated curves have been shifted by 0.025° on the α scale to bring the theory and experimental angular ranges into coincidence. This represents one increment of α in the experiment and is the accuracy with which we can define $\alpha = 0$. Following considerations described in the theory section, and more specifically in Sec. C in the Supplemental Material [40], the error in the thickness is estimated as ±10 Å.

B. Second sample: Si-SiO_2/IL-$CHCl_3$-H_2O

The C, N, F, and B 1s photoelectron peaks from the ionic liquid spacer layer, taken at $\alpha = 2.5°$, are shown in Fig. 9 with best-fit components, the parameters of which are shown in Table I. The C 1s shows two components due to the alkyl chain carbons, C_{alkyl}, and the carbons in the imidazolium region, C_{hetero} [53,54]. The carbon 1s signal from the $CHCl_3$ would be expected to have a binding energy of ≈289.7 eV (≈4.8 eV higher than the alkyl peak [55]) but the intensity is too low to allow it to be distinguished from the high-binding side of imidazolium carbon signal.

The N 1s peak, Fig. 9(b), exhibits two peaks, the higher binding energy peak corresponding to the imidazolium nitrogens in the cation, N_{cat}, and the smaller, lower BE peak to nitrogen in a beam-damaged species, N_{damage} [56]. Figures 9(c) and 9(d) show the fluorine and boron photoelectron peaks, respectively, each fitted with a single component. The two unfitted peaks at ≈198.5 and ≈200.5 eV are due to Cl 2$p_{3/2}$ and 2$p_{1/2}$ photoelectrons from the chloroform marker layer. As the nitrogen peak in the cation shows beam damage we expect the other peaks to also show damage. Although there are no clearly identifiable damage peaks in the C 1s spectra, the C 1s_{hetero} is particularly broad, Table I, indicating there may be intensity changes due to damage within the envelope of the peak. The lack of any damage peaks in the F 1s and B 1s is surprising but may be due to the formation of BF_3 as a damage product, which desorbed and hence did not leave

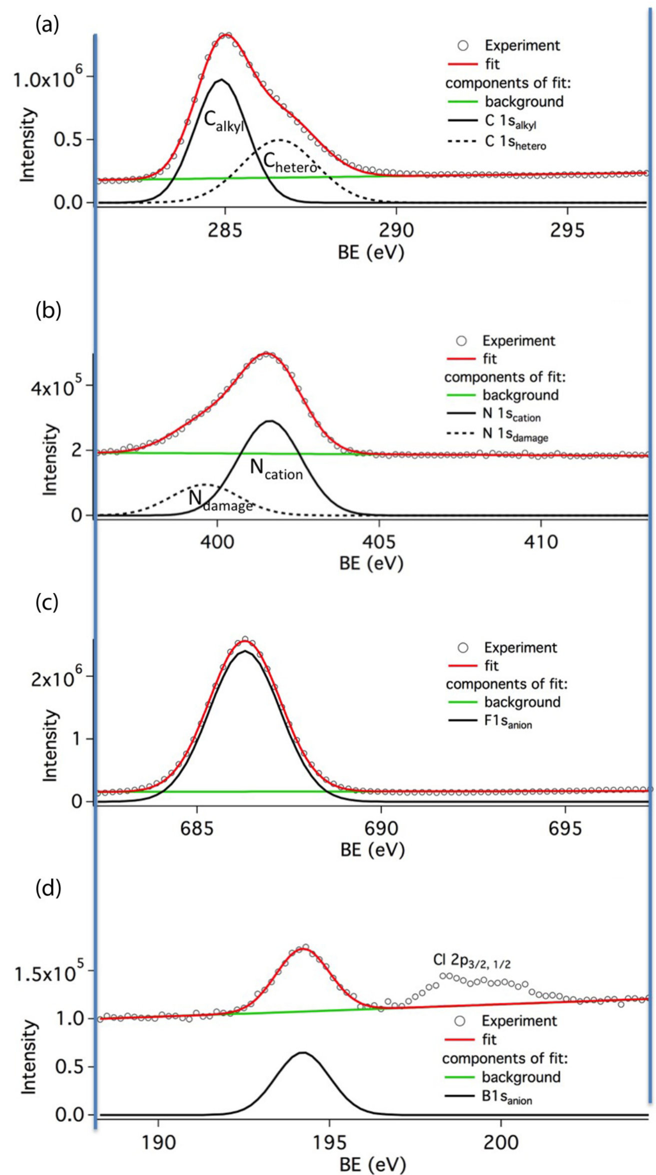

FIG. 9. Photoelectron spectra of [OMIM][BF_4] from the spacer layer of the second sample, Si-SiO_2/IL-$CHCl_3$-H_2O, taken at $\alpha = 2.5°$. (a) C 1s fitted with two components C 1s_{alkyl} and C 1s_{hetero}. (b) N 1s fitted with two components, N 1s_{cat} and N 1s_{damage}. (c) F 1s photoelectron spectrum fitted with a single component. (d) B 1s photoelectron spectrum fitted with a single component.

a peak for XPS to detect. This is discussed later and in the Supplemental Material [40].

For the marker layer surface, the Cl 1s, Fig. 10(a), showed three peaks in the EDC taken at $\alpha = 2.5°$. The middle BE peak, Cl 1s_{CHCl_3} (2823.2 eV BE) can be assigned to undamaged $CHCl_3$ as it was the sole observable peak for EDCs taken at low x-ray exposure times, and it decreased with exposure to the beam. The higher intensity, lower BE peak, Cl 1s_{Cl^-} (2820.9 eV), we assign to a damage product (as it increased with exposure to the beam). As the binding energy is lower than that of $CHCl_3$ we suggest it is due to Cl^-, caused by interaction of $CHCl_3$ and the incident x rays and/or photogenerated electrons. The low intensity, higher BE component, Cl 1$s_{Cl\bullet}$

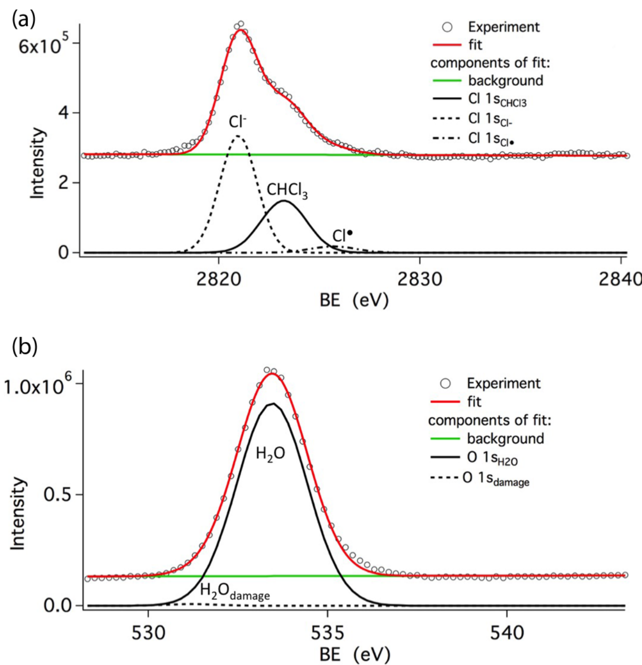

FIG. 10. Photoelectron spectra of [OMIM][BF_4] from the marker layer of the second thin film sample, taken at $\alpha = 2.5^{\circ}$. (a) Cl 1s fitted with three components, Cl $1s_{CHCl_3}$, Cl $1s_{Cl^-}$, and Cl $1s_{Cl\bullet}$. (b) O 1s fitted with two components O $1s_{H_2O}$ and O $1s_{damage}$. All fitting parameters are listed in Table I.

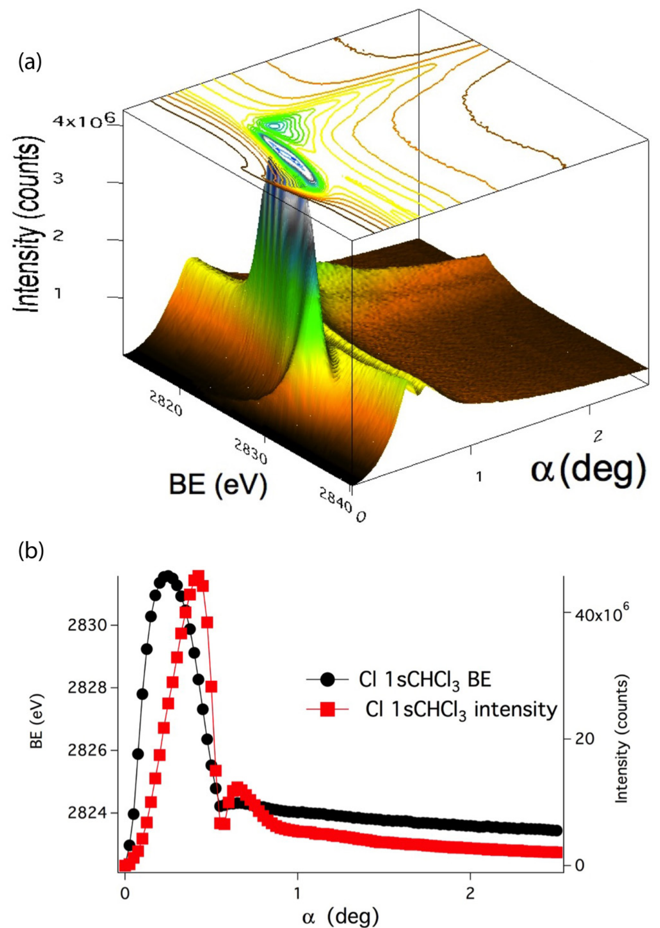

FIG. 11. Experimental results for thin film of $CHCl_3/H_2O$ on IL on Si/SiO_2. (a) VPXSW data as Cl 1s photoelectron intensity versus BE and α and as a contour plot. (b) BE and intensity of the Cl $1s_{CHCl_3}$ component after fitting the data in (a).

(2825.6 eV), we identify as due to approximately neutral chlorine, perhaps due to chlorine atoms, or Cl_2 which had formed from chlorine atoms and was trapped or stabilized within the solid IL. The O 1s spectrum from water in the marker layer, Fig. 10(b), showed one peak due to adsorbed water, O $1s_{H_2O}$, and a very small peak O $1s_{damage}$ which became clearly visible at some angles, which we cannot further identify. The O $1s_{SiO_2}$ peak was not observed as it was too attenuated by the spacer layer to contribute to the spectrum.

Figure 11(a) shows the VPXSW data for chlorine as EDCs stacked to form a 3D plot of electron intensity versus binding energy (BE) and α. The same fitting procedure as described above was used but allowing the BEs and widths to change to accommodate peak movement. The Cl $1s_{CHCl_3}$ peak becomes visible at a BE $\approx$2822.4 eV. As the angle of incidence increases, the peak increases in intensity and moves to higher BE. It then reverses direction and decreases in BE while the intensity continues to increase to a maximum [most easily seen in the contour plot of Fig. 11(a)]. Figure 11(b) shows the BE and intensity of this peak after fitting. The BE maximizes at a value 9.3 eV higher than its starting value at $\alpha \approx 0.25^{\circ}$ while the intensity maximizes at $\alpha \approx 0.42^{\circ}$, and both drop to a local minimum at $\approx$0.55° beyond which the BE only changes very slightly. This behavior of the binding energy may be interpreted as follows. At 90 K the IL slab behaves as an insulator, as the ions cannot move to conduct current, and hence the adlayer is prone to charging by loss of electrons under the action of photoemission. The initial increase in BE is due to positive charging of the organic layer as the evanescent x-ray wave at the vacuum/organic layer interface penetrates further into the organic layer as α increases, causing greater photoemission of electrons. The maximum intensity of the Cl 1s peak coincides with the critical angle of the vacuum/organic layer interface (0.4274°) where the refracted x ray travels parallel to the surface and within the chloroform marker layer (ray $I_{c,P,2}$ in Fig. 2), giving it a maximum path length, and hence maximum absorption and photoelectron intensity. The angle at which photoelectron intensity reaches a minimum and the BE abruptly flattens is close to the critical angle of the organic/SiO_2 interface (0.5828°) where the refracted x-ray wave runs along the IL/SiO_2 interface and hence the intensity in the marker layer is greatly reduced. Interestingly, maximum charging as indicated by the maximum shift in binding energy occurred at a significantly smaller angle than maximum photoemission. We would expect maximum charging to occur when the total electron flux leaving the sample is a maximum, which is not necessarily the same angle at which the Cl 1s adsorbate photoelectron flux maximizes. Unfortunately the drain current, which is the same as the total electron flux leaving the sample, was not monitored in this work, so we are unable to verify whether the charging does maximize at the same angle at which emission of all electrons reaches a maximum.

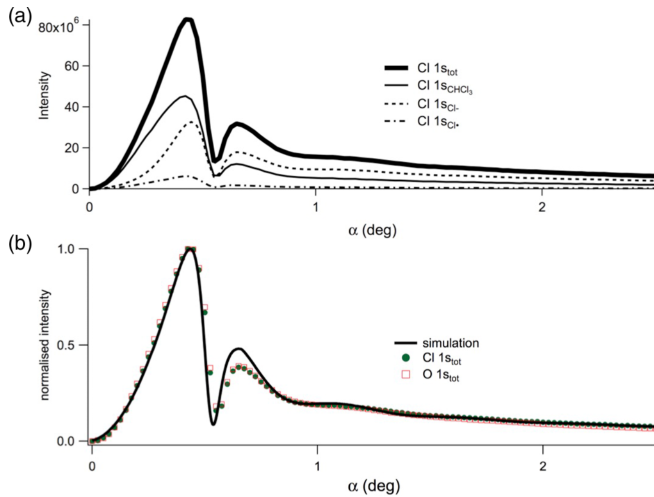

FIG. 12. VPXSW scans for the multilayer surface obtained using Cl and O 1s photoelectron peaks. (a) Intensity versus α for the Cl $1s_{\mathrm{CHCl_3}}$, Cl $1s_{\mathrm{Cl^-}}$, Cl $1s_{\mathrm{Cl\bullet}}$, and Cl $1s_{\mathrm{tot}}$. (b) Cl $1s_{\mathrm{tot}}$ and O $1s_{\mathrm{tot}}$ intensities and the best-fit VPXSW simulation for a surface consisting of a $CHCl_3$-H_2O layer 12 Å thick with its outer surface 223 Å away from the SiO_2 surface. Simulation (corrected for footprint, path length, and shifted by 0.025°) used $\lambda = 9$ Å.

The VPXSW scans of the chemically shifted chlorine components, Cl $1s_{\mathrm{CHCl_3}}$, Cl $1s_{\mathrm{Cl^-}}$, and Cl $1s_{\mathrm{Cl\bullet}}$, are shown in Fig. 12(a) as fitted intensity versus α. The intensity of the $CHCl_3$ component rises quickly to a maximum at 0.43° and is more intense than the Cl^- component. By 0.55° they have the same intensity and to higher angles the Cl^- is the more intense component [see Fig. 10(a) for the components at $\alpha = 2.5°$]. This is consistent with the chloroform cracking under the x-ray beam, but as the standing wave intensity is the primary source of the cracking, the major x-ray dose occurs over the range 0–0.55° beyond which the x-ray intensity settles to much lower values. This means the major changes in the $CHCl_3$ (decreasing) and Cl^- (increasing) occur over the initial part of the scan. The Cl• component has a shape very similar to $CHCl_3$ except for $\alpha < 0.43°$. We interpret this as Cl• being a damage product of $CHCl_3$ which undergoes further beam damage to produce Cl^-. This means that Cl• is a reactive intermediate which will have a low concentration equal to a fixed fraction of the $CHCl_3$ concentration. The reaction sequence assuming the secondary electron flux as the cause of damage is

$$CHCl_3 + e^- \rightarrow Cl\bullet + \text{other products}, \tag{8}$$

$$Cl\bullet + e^- \rightarrow Cl^-. \tag{9}$$

As the sample is at 90 K the damage products are unlikely to be able to diffuse more than a few Å from the position of the original $CHCl_3$ species. The intensities of the three species have therefore been summed, Fig. 12(a), to produce a single VPXSW curve for fitting.

1. *VPXSW of the* $CHCl_3$-H_2O *marker layer*

Figure 12(b) shows the Cl $1s_{\mathrm{tot}}$ and O $1s_{\mathrm{tot}}$ VPXSW scans, normalized to 1 at their maxima, versus α. Within experimental error both curves are the same, as expected if the H_2O and $CHCl_3$ are in a thin marker layer on top of the IL spacer layer. Both exhibit a rapid rise for $\alpha < \alpha_{2,\mathrm{crit}}$ due to the high-intensity part of the standing wave reaching the outmost parts of the surface first, Fig. 12(b), and both signals oscillate for $\alpha > \alpha_{2,\mathrm{crit}}$ because both layers are thin and on the outside of the IL spacer layer where variations in the x-ray standing wave intensity are most pronounced. The best fit is shown in Fig. 12(b) for a combined marker layer of $CHCl_3$ and H_2O with $t = 12 \pm 10$ Å thick, with its outer surface located at 223 ± 15 Å from the substrate surface; see schematic in Fig. 6(b). The simulation used $\lambda = 9$ Å for Cl 1s photoelectrons and $\lambda = 55$ Å for the O 1s photoelectrons. A full estimation of errors is given in Sec. C in the Supplemental Material [40]. The experimental data are less modulated than the simulation at the second oscillation suggesting a level of disorder within the experimental surface which is not simulated. Disorder, either static or dynamic (i.e., thermal), or both, could be incorporated into the simulations, but for the present study the simulations maintain perfect ordering.

2. *VPXSW of the IL spacer layer*

The VPXSW curves obtained using the two components of carbon from the IL, C $1s_{\mathrm{alkyl}}$ and C $1s_{\mathrm{hetero}}$, are shown in Fig. 13(a). Although similar, they differ in relative intensities below 0.5° which is consistent with a buildup of beam damage products within the envelope of peaks in the EDCs [see Fig. 9(a)] which disturbs the apparent relative amounts of the two carbon components. Using the same assumption as for chloroform, above, that the damage products are unlikely to move more than a few Å from their site of production, the total carbon signal, C $1s_{\mathrm{tot}}$, has been used for subsequent analysis.

The VPXSW curves for carbon (C $1s_{\mathrm{tot}}$), fluorine (F 1s), nitrogen (N $1s_{\mathrm{tot}}$), and boron (B 1s) are shown in Fig. 13(b), where N $1s_{\mathrm{tot}}$ is the total intensity of the nitrogen peak, and fluorine and boron are just the intensities of the single peaks. The C, N, and F VPXSW scans are the same within experimental error, while the B curve is similar, but has a slower onset at low angles and less of a peak at ≈0.7°. We attribute the similarity of the C, N, and F scans to the IL spacer layer being homogeneous, consisting of randomly orientated ion pairs which stuck where they landed at the deposition temperature of 90 K, giving a flat distribution of the elements across the depth of the layer. The best fit to the C, N, and F curves, Fig. 13(b), was obtained for a total thickness of 223 ± 15 Å consisting of an IL slab of thickness 211 Å, with a photoelectron empty marker layer of $CHCl_3$-H_2O 12 ± 10 Å thick on top, using an average value of $\lambda = 55$ Å. Although the marker layer does contain carbon from the $CHCl_3$, the carbon density is <0.27 of that in the spacer layer, and it was not detected in the EDCs, so here it has been set equal to zero. An estimation of errors can be found in Sec. C in the Supplemental Material [40]. These distances are entirely consistent with the VPXSW analysis from the $CHCl_3$ and H_2O marker layers.

The VPXSW scan for boron might have been expected to behave the same as for C, N, and F, as it too would have been deposited evenly throughout the spacer layer. However, the boron curve rises more slowly than the other components in

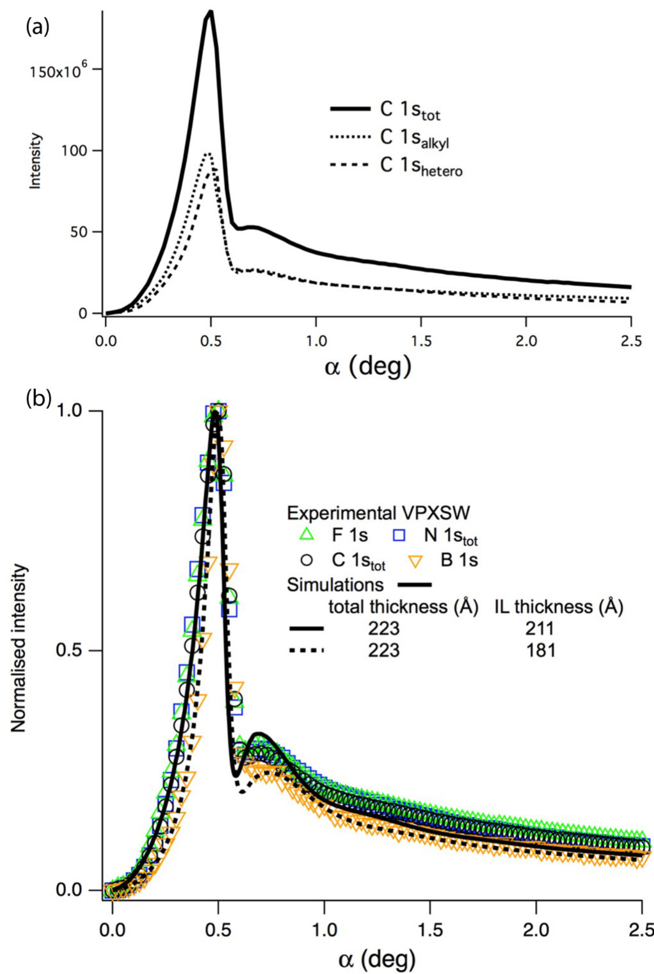

FIG. 13. Experimental and simulated VPXSW curves for the IL layer. (a) Experimental data using the C $1s_{\rm alkyl}$ and C $1s_{\rm hetero}$ components and their sum, C $1s_{\rm tot}$. (b) Experimental data using F $1s$, N $1s_{\rm tot}$, C $1s_{\rm tot}$, and B $1s$ photoelectron intensities and simulations using a total thickness of 223 Å and IL layer thicknesses of 211 Å and 181 Å. Simulations (corrected for x-ray footprint, path length, and shifted by 0.025°) used $\lambda = 55$ Å.

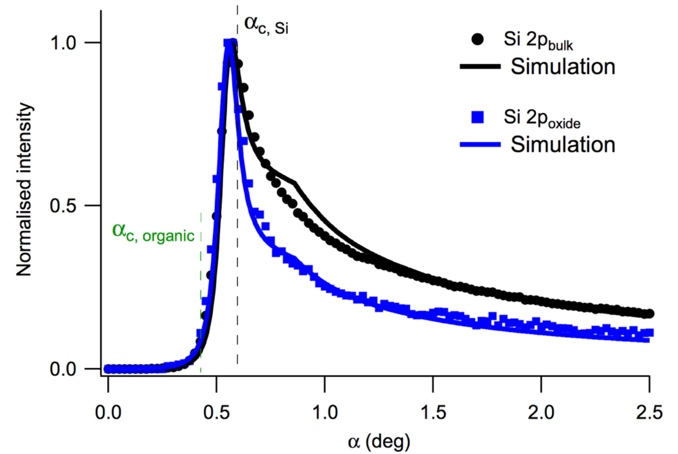

FIG. 14. VPXSW scans of Si $2p$ intensities (sum of $2p_{3/2}$ and $2p_{1/2}$) for bulk Si bulk and SiO_2 lying beneath the organic layer, sample 2. The simulations (normalized to 1, corrected for footprint and path length) used $\lambda = 58$ Å for transmission through bulk Si and SiO_2, an oxide layer 20 Å thick, and an organic layer 223 Å thick. See cartoon in Fig. 6(b). The critical angles of the bulk silicon and organic layers are also shown.

the IL at low angles and has a less pronounced peak at 0.7°. This would be consistent with the loss of BF_3 gas from the surface [57]. The anion $[BF_4]^-$ can react with holes generated by the x radiation [58] to form BF_3 which is sufficiently volatile at 90 K to desorb. This would have the effect of reducing the amount of boron in the topmost layers of the IL spacer layer, equivalent to increasing the depth of the marker layer for which no boron is present. Figure 13(b) shows a VPXSW simulation where the boron in the spacer layer has been reduced to a thickness of 181 Å while keeping the total adlayer thickness at 223 Å. The fit is quite good, supporting the loss of boron from the top ≈30 Å of the IL spacer layer as being the cause for the different behavior of this curve. See Fig. 6(b) for a cartoon of the surface, and Sec. B in the Supplemental Material [40] for a description of the beam damage to $[BF_4]^-$.

The silicon peaks from the Si-SiO_2 substrate were sufficiently penetrating that they had a measurable intensity when a higher pass energy (500 eV) was used on the CHA. VPXSW scans were taken using the Si $2p$ photoelectron peaks, and fitted using $2p_{3/2}$ and $2p_{1/2}$ components for both the bulk and oxide. Figure 14 shows the VPXSW curves plotted as the sum of the spin-orbit split components for the bulk and the oxide. Both have almost no intensity below the critical angle of the organic layer, and then rise rapidly to a maximum at the silicon critical angle. To higher angles the oxide signal drops more quickly than the bulk signal due to the x rays penetrating into the bulk silicon at greater angles and hence producing a greater flux of photoelectrons. Also shown in Fig. 14 are two simulated curves. Both used a total organic layer thickness of 223 Å, as derived from the above analysis, a λ value of 58 Å through the bulk silicon and SiO_2, and a slightly increased x-ray beam diameter to the CHA focal spot diameter ratio of 0.015 due to the higher pass energy used. The attenuation of both the bulk Si and SiO_2 photoelectron fluxes as they pass through the overlying organic layer remains constant with respect to angle, and hence need not be calculated making the value of λ for the organic layer irrelevant here. For the oxide simulation a marker layer 20 Å thick was used (as determined above), lying between the bulk silicon and the organic layer. The fits to both the oxide and the bulk curves are good. The kinks in both simulations at ≈0.85° are due to the rather simple footprint correction used here, the value of the correction changing abruptly as the x-ray footprint exceeds the CHA field of view at low angles, causing the kink. A more realistic, smoothed, transition could be used in later work. From this it can be seen that the thicknesses found using the $CHCl_3$-H_2O marker layer signals and the ionic liquid spacer layer signals also fit the signals from the bulk silicon and the SiO_2 layer that lie below the organic layer.

3. *Surface roughness*

For the photoelectron signals originating from the Si-SiO_2 surface in contact with the vacuum (sample 1) or in

contact with the spacer layer above it (sample 2), there were no discernible differences between the calculated VPXSW curve (which uses perfectly flat interfaces) and experimental VPXSW curves (where there must be interface roughness). This indicates that any effects due to interface roughness were not apparent due to the experimental noise. However, for photoelectron signals from the ionic liquid spacer layer and $CHCl_3/H_2O$ marker layer VPXSW curves, Figs. 12 and 13, the intensity variations in the experiment were less than those in the simulations indicating an observable effect of roughness in the spacer layer/marker layer/vacuum interfaces. Roughness in reflectivity measurements is usually defined as a Gaussian distribution of surface facet heights about the mean average surface for the substrate, with a root mean square value of σ. It can be defined for each interface in the system, with (usually) much larger distributions for adsorbate interfaces above the substrate. The effect of these roughness distributions on the measured fluorescence yield in variable-period x-ray standing waves has been extensively discussed by Zhang *et al.* [25], who show that the VPXSW oscillations are broadened and dampened. In the present work roughness at the substrate as well as the adsorbate interfaces will affect the spatial extent of the x-ray standing wave which initiates photoelectron emission as well as affecting the measured photoelectron intensity via attenuation across the rough regions. To obtain an approximate value for the spacer layer roughness the average of nine discrete simulations for varying thicknesses of the spacer layer were calculated while keeping the marker layer thickness fixed at 12 Å. The average simulations approximately matched the reduced oscillations of the experimental C and O signals in the marker layer and the B, C, N, and F signals in the spacer layer. The roughness needed to achieve this was $\sigma \approx 40$ Å. A later work will address the roughness more accurately.

V. CONCLUSIONS

Variable-period x-ray standing wave experiments have been carried out using photoelectron detection. 3 keV x rays were reflected from a polished silicon surface over an angular range of 2.5°. Two surface layer structures were studied: the native oxide of silicon on a bulk silicon substrate, and a purpose-built model surface consisting of a native oxide/silicon as a substrate, surmounted by a spacer layer of solid [OMIM][BF_4], which terminated in a marker layer composed of $CHCl_3$ and H_2O. VPXSW data were obtained by monitoring the photoelectron intensities of Si $2p_{1/2,3/2}$ and O 1*s* for the SiO_2/Si surface, and of Si $2p_{1/2,3/2}$ and B, C, N, O, F, and Cl 1*s* for the Si-SiO_2/[OMIM][BF_4]-$CHCl_3$-H_2O surface (spanning kinetic energies of 100–2830 eV). The VPXSW scans were analyzed by modeling them using dynamical x-ray theory and a three-layer system, vacuum/adsorbate layer/substrate layer, to determine the x-ray intensities within the adsorbate and the substrate, the Beer-Lambert law and appropriate attenuation lengths to model photoelectron emission along the surface normal, and two corrections, for x-ray path length through the surface layers and the footprint of the x ray relative to the field of view of the electron energy analyzer. The SiO_2 film was found to comprise a layer 20 ± 10 Å thick using three independent photoelectron measurements, Si $2p_{1/2,3/2}$ from the bulk and from the surface SiO_2, and O 1*s* from the SiO_2. For the combined $CHCl_3/H_2O$ marker layer surface, the thickness (12 ± 10 Å) and position of the outside surface (223 ± 15 Å) were found using the high-energy O 1*s* and the low-energy Cl 1*s* photoelectron peaks. The thickness of the ionic liquid spacer layer was found to be 211 ± 15 Å using the C, N, and F 1*s* photoelectron peaks. This is entirely compatible with the marker layer thickness. The total thickness of the spacer and marker layers (223 Å) determined using the bulk Si $2p_{1/2,3/2}$ photoelectron signal that had passed through them was consistent with the other measurements. The high-intensity x-ray beam running parallel to the surface at the critical angle of the organic layer resulted in beam damage to all three components, [OMIM][BF_4], $CHCl_3$, and H_2O. The damage product, BF_3, from [BF_4]$^-$ was thought to escape from the surface giving a boron VPXSW curve characteristic of a 30 Å thick layer, depleted of boron, in the outmost part of the IL. The high flux of photoelectrons also led to substantial charging (9.3 eV) of the insulating organic layer. The depth accessible to measurement here, using photoelectrons from 3 keV photons, is $\lesssim$300 Å. The accuracy for determining the position of a marker layer and the thickness of a slab are about 10 Å and 15 Å, respectively, while the accuracy of determining marker layer thicknesses is about 10 Å. Chemical shifts in the photoelectron peaks clearly showed that chemical state specificity is easily achieved. Future work should be capable of determining an arbitrary density distribution through an adlayer by combining VPXSW data with different electron attenuation lengths obtained using different x-ray energies. Other possibilities also exist to carry out spatially resolved near-edge x-ray absorption fine structure studies.

ACKNOWLEDGMENTS

Funding from the Engineering and Physical Sciences Research Council, UK (EP/I018093/1), synchrotron beam time from Diamond Light Source (SI 9118), and support from a Ph.D. studentship from School of Chemistry, Nottingham (J.S.G.), are gratefully acknowledged. We thank P. Licence for providing the ionic liquid.

[1] E. Langereis, S. B. S. Heil, H. C. M. Knoops, W. Keuning, M. C. M. van de Sanden, and W. M. M. Kessels, J. Phys. D: Appl. Phys. **42**, 073001 (2009).
[2] D. E. Aspnes, Thin Solid Films **571**, 334 (2014).
[3] M. Losurdo *et al.*, J. Nanopart. Res. **11**, 1521 (2009).
[4] E. Chason and T. M. Mayer, Crit. Rev. Solid State Mater. Sci. **22**, 1 (1997).
[5] J. C. Vickerman and D. Briggs, *ToF-SIMS: Materials Analysis by Mass Spectrometry* (IM Publications, Chichester, UK and Surface Spectra Limited, Manchester, UK, 2013).

[6] P. J. Cumpson, J. Electron Spectrosc. Relat. Phenom. **73**, 25 (1995).
[7] J. Zegenhagen and A. Kazimirov (eds.), *The X-Ray Standing Wave Technique: Principles and Applications* (World Scientific, Singapore, 2013).
[8] D. P. Woodruff, Rep. Prog. Phys. **68**, 743 (2005).
[9] S. H. Yang, A. X. Gray, A. M. Kaiser, B. S. Mun, B. C. Sell, J. B. Kortright, and C. S. Fadley, J. Appl. Phys. **113**, 073513 (2013).
[10] C. Papp, G. Conti, B. Balke, S. Ueda, Y. Yamashita, H. Yoshikawa, Y. S. Uritsky, K. Kobayashi, and C. S. Fadley, J. Appl. Phys. **112**, 114501 (2012).
[11] A. von Bohlen, Spectrochim. Acta, Part B **64**, 821 (2009).
[12] R. G. Jones *et al.*, J. Phys.: Condens. Matter **14**, 4059 (2002).
[13] R. G. Jones, I. Shuttleworth, C. J. Fisher, J. J. Lee, S. L. Bastow, R. Ithnin, J. Ludecke, M. P. Skegg, D. P. Woodruff, and B. C. C. Cowie, in *Physics of Low-Dimensional Structures*, 3rd International Conference on Physics of Low-Dimensional Structures, Chernogolovka, Russia (VSV Co. Ltd, Moscow, Russia, 2001), Vol. 11-2, pp. 1–26.
[14] D. P. Woodruff, Prog. Surf. Sci. **57**, 1 (1998).
[15] J. Zegenhagen, Surf. Sci. Rep. **18**, 202 (1993).
[16] D. P. Woodruff, B. C. C. Cowie, and A. Ettema, J. Phys.: Condens. Matter **6**, 10633 (1994).
[17] M. J. Bedzyk, G. M. Bommarito, and J. S. Schildkraut, Phys. Rev. Lett. **62**, 1376 (1989).
[18] M. J. Bedzyk, in *The X-Ray Standing Wave Technique* (World Scientific, Singapore, 2013), p. 94.
[19] Z. Erdelyi *et al.*, X-Ray Spectrom. **38**, 338 (2009).
[20] R. Itri, R. T. Zhang, and M. Caffrey, Biophys. J. **73**, 1506 (1997).
[21] M. Kraemer, A. von Bohlen, C. Sternemann, M. Paulus, and R. Hergenroeder, J. Anal. At. Spectrom. **21**, 1136 (2006).
[22] M. Kraemer, A. von Bohlen, C. Sternemann, M. Paulus, and R. Hergenroeder, Appl. Surf. Sci. **253**, 3533 (2007).
[23] J. Wang, M. J. Bedzyk, T. L. Penner, and M. Caffrey, Nature (London) **354**, 377 (1991).
[24] J. Wang, M. Caffrey, M. J. Bedzyk, and T. L. Penner, J. Phys. Chem. **98**, 10957 (1994).
[25] R. T. Zhang, R. Itri, and M. Caffrey, Biophys. J. **74**, 1924 (1998).
[26] M. Mehta and C. S. Fadley, Phys. Lett. A **55**, 59 (1975).
[27] M. Mehta and C. S. Fadley, Chem. Phys. Lett. **46**, 225 (1977).
[28] J. Kawai, M. Takami, M. Fujinami, Y. Hashiguchi, S. Hayakawa, and Y. Gohshi, Spectrochim. Acta, Part B **47**, 983 (1992).
[29] J. Kawai, S. Hayakawa, Y. Kitajima, K. Maeda, and Y. Gohshi, J. Electron Spectrosc. Relat. Phenom. **76**, 313 (1995).
[30] J. Kawai, S. Kawato, K. Hayashi, T. Horiuchi, K. Matsushige, and Y. Kitajima, Appl. Phys. Lett. **67**, 3889 (1995).
[31] J. Kawai, J. Electron Spectrosc. Relat. Phenom. **178–179**, 268 (2010).
[32] M. J. Chester and T. Jach, Phys. Rev. B **48**, 17262 (1993).
[33] M. J. Chester, T. Jach, and S. Thurgate, J. Vac. Sci. Technol. B **11**, 1609 (1993).
[34] T. Jach, J. Gormley, and S. Thurgate, Spectrochim. Acta, Part B **54**, 1539 (1999).
[35] T. Jach and E. Landree, J. Surf. Anal. **9**, 339 (2002).
[36] T. Jach, J. A. Dura, N. V. Nguyen, J. Swider, G. Cappello, and C. Richter, Surf. Interface Anal. **36**, 23 (2004).
[37] E. Landree, T. Jach, D. Brady, A. Karamcheti, J. Canterbury, W. Chism, and A. C. Diebold, in *Characterization and Metrology for ULSI Technology 2000, International Conference*, edited byD. G. Seller, A. C. Diebold, T. J. Shaffner, R. McDonald, W. M. Bullis, P. J. Smith, and E. M. Secula (American Institute of Physics, Melville, NY, 2001), p. 159.
[38] D. P. Woodruff and T. A. Delchar., *Modern Techniques of Surface Science* (Cambridge University Press, Cambridge, UK, 1994).
[39] B. L. Henke, E. M. Gullikson, and J. C. Davis, At. Data Nucl. Data Tables **54**, 181 (1993).
[40] See Supplemental Material at http://link.aps.org/supplemental/10.1103/PhysRevB.98.165402 for Sec. A, x-ray constants; Sec. B, possible desorption of BF_3 damage products from a 90 K surface; and Sec. C, estimate of errors in fittings.
[41] D. Briggs and J. T. Grant, editors, *Surface Analysis by Auger and X-Ray Photoelectron Spectroscopy* (IM Publications, Chichester, 2003).
[42] C. J. Powell and A. Jablonski, NIST Electron Inelastic-Mean-Free-Path Database, Version 1.2, National Institute of Standards and Technology, Gaithersburg, MD, 2010.
[43] R. G. Jones (private communication).
[44] R. Foulston, S. Gangopadhyay, C. Chiutu, P. Moriarty, and R. G. Jones, Phy. Chem. Chem. Phys. **14**, 6054 (2012).
[45] M. Buckley, Ph.D. thesis, University of Nottingham, 2016.
[46] C. J. Fisher, R. Ithin, R. G. Jones, G. J. Jackson, D. P. Woodruff, and B. C. C. Cowie, J. Phys.: Condens. Matter **10**, L623 (1998).
[47] J. J. Lee, C. J. Fisher, D. P. Woodruff, M. G. Roper, R. G. Jones, and B. C. C. Cowie, Surf. Sci. **494**, 166 (2001).
[48] R. G. Jones (private communication).
[49] D. N. Belton, S. J. Harris, S. J. Schmieg, A. M. Weiner, and T. A. Perry, Appl. Phys. Lett. **54**, 416 (1989).
[50] G. B. Hoflund, D. A. Asbury, C. F. Corallo, and G. R. Corallo, J. Vac. Sci. Technol. A **6**, 70 (1988).
[51] C. J. Powell and A. Jablonski, J. Phys. Chem. Ref. Data **28**, 19 (1999).
[52] A. C. Thompson and D. Vaughan, editors, *X-Ray Data Booklet* (Lawrence Berkeley National Laboratory, Berkeley, California, 2001).
[53] E. F. Smith, F. J. M. Rutten, I. J. Villar-Garcia, D. Briggs, and P. Licence, Langmuir **22**, 9386 (2006).
[54] I. J. Villar-Garcia, E. F. Smith, A. W. Taylor, F. Qiu, K. R. J. Lovelock, R. G. Jones, and P. Licence, Phys. Chem. Chem. Phys. **13**, 2797 (2011).
[55] U. Gelius, P. F. Hedén, J. Hedman, B. J. Lindberg, R. Manne, R. Nordberg, C. Nordling, and K. Siegbahn, Phys. Scr. **2**, 70 (1970).
[56] K. R. J. Lovelock, E. F. Smith, A. Deyko, I. J. Villar-Garcia, P. Licence, and R. G. Jones, Chem. Commun. **2007**, 4866 (2007).
[57] NIST Chemistry WebBook, Standard Reference Database Number 69, https://webbook.nist.gov/chemistry.
[58] I. A. Shkrob, T. W. Marin, S. D. Chemerisov, and J. F. Wishart, J. Phys. Chem. B **115**, 3872 (2011).